



**Engineering crack tortuosity in printed polymer-polymer
composites through ordered pores**

Journal:	<i>Materials Horizons</i>
Manuscript ID	MH-COM-02-2020-000331.R1
Article Type:	Communication
Date Submitted by the Author:	13-Apr-2020
Complete List of Authors:	Gockowski, Luke; University of California Santa Barbara, Mechanical Engineering Dolinski, Neil; University of California Santa Barbara, Materials Chavez, Roberto; University of California Santa Barbara, Chemistry and Biochemistry Cohen, Noy; Technion Israel Institute of Technology, Materials Science and Engineering Eisenreich, Fabian; Humboldt-Universitat zu Berlin, Chemistry and IRIS Adlershof Hecht, Stefan; Humboldt-Universitat zu Berlin, Chemistry and IRIS Adlershof McMeeking, Robert; University of California Santa Barbara, Mechanical Engineering and Materials; University of Aberdeen, School of Engineering; Leibniz Institute for New Materials Hawker, Craig; University of California Santa Barbara, Chemistry and Biochemistry, and Materials Valentine, Megan; University of California Santa Barbara, Mechanical Engineering

Engineering crack tortuosity in printed polymer-polymer composites through ordered pores

Luke F. Gockowski^{a,†}, Neil D. Dolinski^{b,†}, Roberto Chavez^c, Noy Cohen^d, Fabian Eisenreich^e, Stefan Hecht^e, Robert M. McMeeking^{a,b,f,g}, Craig J. Hawker^{b,c,*}, and Megan T. Valentine^{a,*}

New Concepts

Nature offers a wealth of composites that exploit hierarchically organized stiff-soft motifs to achieve impressive mechanical properties that have long inspired materials design. Despite their desirable properties, natural materials are challenging to replicate due to their finely arranged and interfaced domains with distinct compositions/properties. While multimaterial 3D printing offers a promising route for emulating the structure, composition, and performance of such natural materials, state-of-the-art processes to produce multimaterial parts are prohibitively complex, costly, and slow for wide adoption by researchers. We present a new approach: by leveraging solution mask liquid lithography (SMaLL), a recently-developed light-controlled single-step multimaterial printing process, we create polymer-polymer composites that capture the key features of porous and multiphasic natural materials. We print structures comprising a stiff exterior surrounding a soft porous core that are naturally bonded at molecular scales, eliminating defects and suppressing delamination at the interface. Through varying the size and packing of the pores, materials that undergo dramatic crack deflection can be produced. These findings offer design rules for creating resilient polymer-polymer composites while demonstrating the potential of SMaLL for manufacturing mechanically complex materials.

COMMUNICATION

Engineering crack tortuosity in printed polymer-polymer composites through ordered pores

Received 00th January 20xx,
Accepted 00th January 20xx

Luke F. Gockowski^{a,†}, Neil D. Dolinski^{b,†}, Roberto Chavez^c, Noy Cohen^d, Fabian Eisenreich^e, Stefan Hecht^e, Robert M. McMeeking^{a,b,f,g}, Craig J. Hawker^{b,c,*}, and Megan T. Valentine^{a,*}

DOI: 10.1039/x0xx00000x

Multimaterial additive manufacturing is an enabling tool for exploring hard to access structure-property relationships. In this work, a recently developed multimaterial printing approach, solution mask liquid lithography, is used to produce porous polymer-polymer composites inspired by tough, hierarchical structures found in nature. The results demonstrate that varying the size and packing of pores in the core structure leads to significant enhancement in crack deflection. Finite element analysis reveals that this enhancement is linked to geometry-dependent stress distribution.

Nature is replete with materials that exhibit mechanical properties that are desirable, yet challenging to emulate. For example, simultaneous toughness and strength can be achieved by using strong interfaces to join soft (e.g., biopolymer) and hard (e.g., mineral) domains^{1–3}. Despite knowledge of these motifs, synthetic strategies for replication/emulation remain inaccessible via traditional manufacturing methods due to the complex synthesis of constituent materials, their hierarchical organization, and a lack of robust techniques to couple mechanically and chemically distinct material domains. The ability to precisely control the structure, composition, and interfaces^{4,5} in multimaterial composites is vital for developing useful synthetic mimics.

New Concepts

Nature offers a wealth of composites that exploit hierarchically organized stiff-soft motifs to achieve impressive mechanical properties that have long inspired materials design. Despite their desirable properties, natural materials are challenging to replicate due to their finely arranged and interfaced domains with distinct compositions/properties. While multimaterial 3D printing offers a promising route for emulating the structure, composition, and performance of such natural materials, state-of-the-art processes to produce multimaterial parts are prohibitively complex, costly, and slow for wide adoption by researchers. We present a new approach: by leveraging solution mask liquid lithography (SMaLL), a recently-developed light-controlled single-step multimaterial printing process, we create polymer-polymer composites that capture the key features of porous and multiphase natural materials. We print structures comprising a stiff exterior surrounding a soft porous core that are naturally bonded at molecular scales, eliminating defects and suppressing delamination at the interface. Through varying the size and packing of the pores, materials that undergo dramatic crack deflection can be produced. These findings offer design rules for creating resilient polymer-polymer composites while demonstrating the potential of SMaLL for manufacturing mechanically complex materials.

New methods for polymer-polymer composite fabrication offer attractive routes for such synthesis—providing control over composition, processability, and manufacturability. For example, researchers have demonstrated enhanced mechanical properties by interfacing macroscopic elastomer structures^{6,7} and woven fibers^{8,9} with polymer gel networks. However, the stepwise synthetic strategies (e.g., casting) used in these works fail to replicate the fine structure of many natural materials. To achieve these demanding designs, much attention has been given to multimaterial 3D printing, which has been used to produce structures that draw bio-inspiration from subjects such as mantis shrimp claws¹⁰, nacre¹¹, bone¹², and a suite of other desirable natural materials^{13,14}. Yet even mature multimaterial 3D printing technologies suffer from significant drawbacks such as cost, complexity, and slow build rates that hinder greater

^a Department of Mechanical Engineering, University of California Santa Barbara, Santa Barbara, CA 93106

^b Materials Department, University of California Santa Barbara, Santa Barbara, CA 93106

^c Department of Chemistry and Biochemistry, University of California Santa Barbara, Santa Barbara, CA 93106

^d Department of Materials Science and Engineering, Technion – Israel Institute of Technology, Haifa 3200003, Israel

^e Department of Chemistry and IRIS Adlershof, Humboldt-Universität zu Berlin, 12489 Berlin, Germany

^f School of Engineering, University of Aberdeen, King's College, Aberdeen AB24 3UE, UK

^g INM - Leibniz Institute for New Materials, 66123 Saarbrücken, Germany

[†] These authors contributed equally to this work

Electronic Supplementary Information (ESI) available: Details of resin preparation, sample design and production, experimental protocols, data analysis, and videos of sample failure. See DOI: 10.1039/x0xx00000x

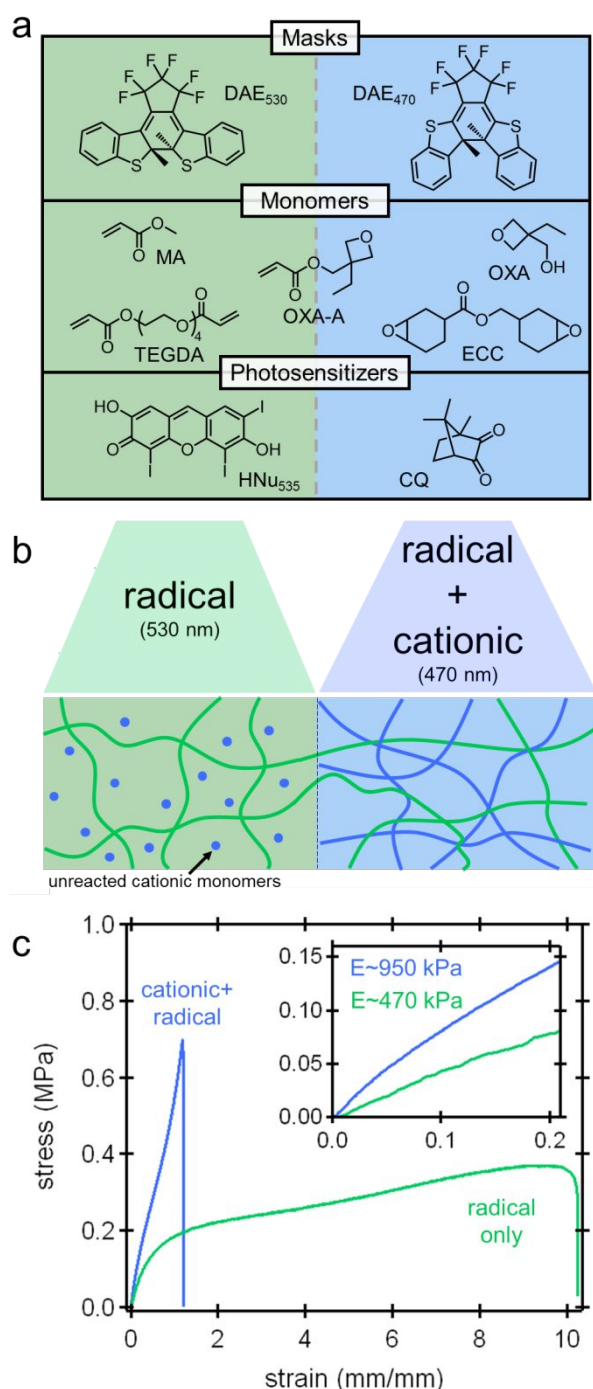


Fig. 1. a) Chemical structures of the major resin components used in this work. b) Schematic network structures resulting from irradiation of the resin with green (530 nm) or blue (470 nm) light. c) Representative (nominal) stress-strain plots of resulting materials after removal of unreacted species.

exploration of bio-inspired structures. While a number of new strategies for the rapid production of 3D printed parts^{15–18} have recently been introduced, these technologies often rely on the use of a single resin stock and thus are incapable of producing multimaterial parts without the need to stop a print to exchange resins. Generally, single-source approaches can be altered for multi-material printing capabilities via variable light

intensity¹⁹, aligned filler particles²⁰, or microfluidic printheads²¹. However, the materials properties of the printed products are usually dictated and/or limited by a single curing chemistry.

To address these shortcomings, a new approach was developed, solution mask liquid lithography (SMaLL), that uses different wavelengths of light to control localized curing chemistries, enabling one-step multimaterial 3D printing.²² SMaLL boasts rapid print speeds (50 cm h⁻¹), high lateral resolution (~100 μm), and importantly the ability to generate polymer-polymer composites with spatially specific and well-defined mechanical properties. As such, SMaLL is uniquely positioned to enable the study of nature-inspired composites with finely-featured and mechanically distinct (stiff-soft) domains. Here, we exploit this advantage to design and test composites composed of a stiff outer layer, soft interior core domain, and controlled pore packing / distribution. Our findings demonstrate that the high fracture-resistance of porous natural composites can be captured in such synthetic mimics and moreover, reveal trends that can be generalized for the design of resilient polymer-polymer composites.

The key innovation in our manufacturing technique is that the single resin used in SMaLL can undergo orthogonal curing reactions triggered by exposure to different wavelengths of light. Here, green (530 nm) and blue (470 nm) light are used to induce different photopolymerizations, resulting in radical and radical plus cationic cured (crosslinked) networks, respectively (full details of formulations and printing conditions can be found in the Supporting Information). Green wavelengths excite the HNU₅₃₅ photosensitizer, triggering solely the radical polymerization of methyl acrylate (MA) monomers and triethylene glycol diacrylate (TEGDA) crosslinkers, while blue light excites the camphorquinone (CQ) photosensitizer, triggering the dual curing of 3-ethyl-3-oxetanemethanol (OXA) monomers and 3,4-epoxycyclohexylmethyl 3,4-epoxycyclohexanecarboxylate (ECC) crosslinkers as well as MA and TEGDA through cationic and radical curing (Fig. 1a,b). Importantly, a small amount (~5 wt%) of network compatibilizer, 3-ethyloxetan-3-yl)methyl acrylate (OXA-A), with both acrylate and oxetane functionalities, is used to prevent phase separation between the radical and cationic networks formed during exposure to blue light. After printing, the samples are swollen several times in acetone/isopropanol, and are subsequently dried, to remove any unreacted molecules. This strategy of dual-wavelength control has recently been extended to operate under UV and visible light, highlighting the flexibility of orthogonal photochemistries for simplified multi-material printing.²³ Critically, the wide range of available polymer and curing chemistries provides a broad palette for materials design, thus enabling a number of tunable properties to be captured in the printed composites.

In addition to providing wavelength-selective polymerization and crosslinking, SMaLL provides exceptionally fast and high-resolution printing through the addition of absorbing species (solution masks) overlapping in absorbance

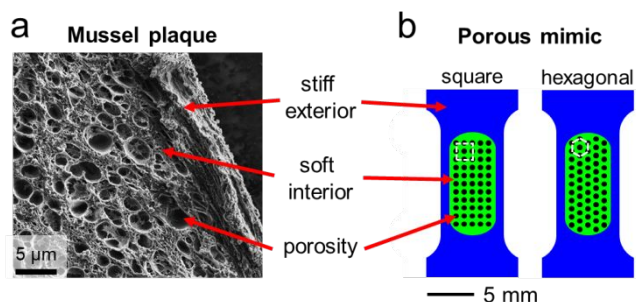


Fig. 2. a) Micrograph of a sectioned mussel plaque, with distinct design elements, such as hierarchical and multiphase features are ubiquitous in biological materials. b) Mimetic templates with blue, green and black regions to define a stiff outer shell, soft interior core, and controlled pores using SMaLL. White shape to emphasize packing of pores

with the photosensitizing species. By using photochromic molecules that switch from highly-absorbing to inert (transparent) states upon light absorption as solution masks, well-defined photobleaching fronts^{24–26} are forced to move through the resin under the control of a user-defined light field, thus allowing for the production of complex multimaterial samples without the need of a moving build stage. In this work, two diarylethene switches, 1,2-bis(2-methyl-1-benzothiophen-3-yl)perfluorocyclopentene (DAE₅₃₀) and 1,2-bis(3-methyl-1-benzothiophen-2-yl)perfluorocyclopentene (DAE₄₇₀), were mixed with the resin described above (Fig. 1a) to mask—and thereby control the propagation of—green and blue light, respectively. Exposure to green light for and subsequent dialysis and drying afforded elastomeric radical-only networks with elastic moduli of 470 kPa and ultimate strains of over 1000%. In contrast, exposure to blue light led to stiffer, and much less extensible, materials with elastic moduli of 950 kPa and ultimate strains of approximately 100% (Fig. 1c). Using color templates comprised of blue and green regions and a commercially-available projector, materials consisting of both components can be readily produced in a single step (see Supporting Information Section 1E). Importantly, this single

step fabrication creates multiphase composites without the need to bond two dissimilar materials and thereby minimizes the presence of defects at the interface that tend to nucleate cracks and undermine strength.

Examples of hierarchical multiphase materials are ubiquitous in biology. Notable examples include stiff and fracture-resistant trabecular bone^{27,28}, the resilient soft solids that comprise multicellular tissues^{29–31}, complex biofilms comprising microbes in a soft matrix³², and the extracellular adhesives produced by marine mussels³³. In particular, the natural materials produced by mussels have garnered significant interest for their relative strength and remarkable ability to adhere to a variety of surfaces in wet, turbulent intertidal zones. The structure-property relationships of the mussel's holdfasts have been examined^{34–36}, and their unique toughness^{37,38}, adhesion ability^{39–42}, and biochemistry^{41,43} have been thoroughly characterized and mussel-inspired materials with notable mechanical performance^{44,45} have been developed. However, prior designs of mussel-mimetic materials rarely consider the material composition and structure of the natural material (Fig. 2a), despite its hypothesized role in the toughness of the mussel's load-bearing holdfasts.^{37,46,47} Inspired by such design motifs, polymer-polymer composites comprising a stiff 'shell' and a soft porous 'core' with defined pore sizes and packing orientations (Fig. 2b) were designed, printed using SMaLL, and tensile tested. The stiff and soft domains exhibit distinct mechanical responses—i.e., a two-fold difference in elastic moduli, a nearly ten-fold difference in extensions to failure, and distinct yield behaviors—yet are covalently linked through a shared radically-cured acrylate network.²² Based on these design features, samples with an outer shell defined by blue light and an interior core with porosity defined by green light were prepared. In addition, the pore size and pore packing order were varied to uncover structure-property relationships that in turn inform fracture-resistant composite design. To this end, samples with mean pore diameters of 1600, 1300, and

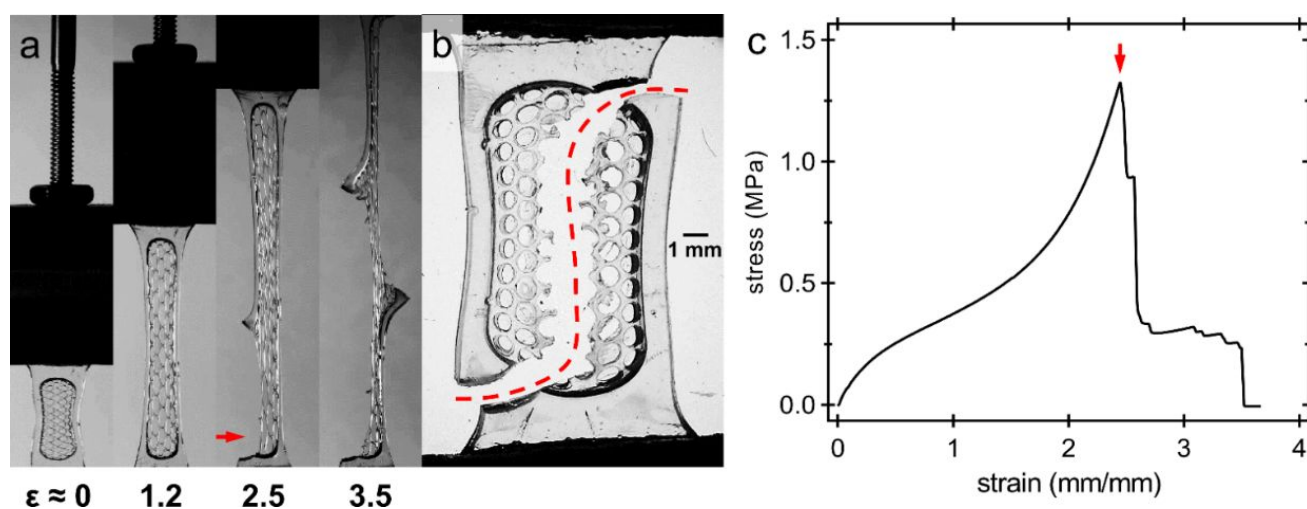


Fig. 3. Results from the uniaxial loading of a pristine sample with hexagonally packed 1000 μm voids. a) Still-frames of the sample under increasing strain. b) Optical microscope image of the fractured part, demonstrating a high degree of crack tortuosity. c) The (nominal) stress-strain plot corresponding to parts a/b, showing distinct failure events after the onset of crack propagation (arrow) that correspond to the breaking of individual ligaments within the material.

1000 μm were patterned into either hexagonal- or square-packed lattices (Fig. S2). To simplify the comparison between samples, the area fraction of pores was held constant ($51 \pm 3\%$).

To establish a benchmark mechanical response, samples devoid of pores were first examined. For all specimens, at some critical load, cracks in these samples consistently initiated at the exterior of the sample and rapidly propagated linearly across the sample, perpendicular to the axis of load, until they exited through the opposite side (Fig. S8 and Movie S1). The lack of porosity in the soft interior of the sample eliminates any possibility for crack blunting or stress dissipation—allowing the crack to propagate through the sample uninhibited. Conversely, samples containing patterned pores exhibit a large degree of crack deflection. Further tensile tests revealed that porous samples experience highly non-linear or tortuous crack propagation (Fig. 3a) based on pore size and orientation (Fig. S3). An extreme case of this behavior is seen in a hexagonally-packed, 1000- μm pore sample whose fatal crack pivots ninety degrees twice before exiting the sample (Fig. 3b and Movie S2). In this example, a crack forms at 250% strain near the bottom of one end of the sample, followed shortly thereafter by a nearly-identical, diagonally-opposed crack in the exterior shell at the opposing end. Instead of leading to the immediate failure of the sample, however, the pores momentarily halt crack propagation and the sample rotates and shear in the soft porous core of the fracturing specimen forces the diagonally-opposed cracks to pivot ninety degrees until they meet in the middle of the soft core, causing failure nearly 100% strain after the point of initiation (Fig. 3c). Despite the encouraging changes in failure behavior and remarkable reorganization enabled by deformation and scission of the thin struts forming the pore walls of the inner core, tests investigating the relationship between crack tortuosity and pore size/packing were inconclusive due to the stochasticity of crack initiation (Fig. S3-S4).

To more accurately assess the impact of porosity and multimaterial composition, notches were designed and printed into in the outer shell of each sample near a centrally-located pore, thus creating a controlled point of crack initiation. Using notched samples, systems with square-packed pores were found to undergo less tortuous crack paths when compared to their hexagonally-packed counterparts (Fig. 4a,b, and Figs. S6-7). Furthermore, the increased tortuosity in the hexagonally-packed samples often led to enhancements in strains to failure (Fig. 4c and Movie S3). In each case, we quantify the degree of tortuosity of the crack paths by dividing the length of the crack by the width of the sample at its notch point (i.e., c_{norm}). For example, a crack that propagates from its notch point straight across the sample will have a normalized crack length value of $c_{\text{norm}} = 1$, while a crack that deviates from this linear path will have a $c_{\text{norm}} > 1$. Using this metric, it was found that, irrespective of pore size, all samples with square-packed pores endured near-linear crack paths (Fig. 5), similar to the results obtained in the pore-free samples. Conversely, cracks in the hexagonally-packed samples showed a clear increase in tortuosity with decreasing pore size.

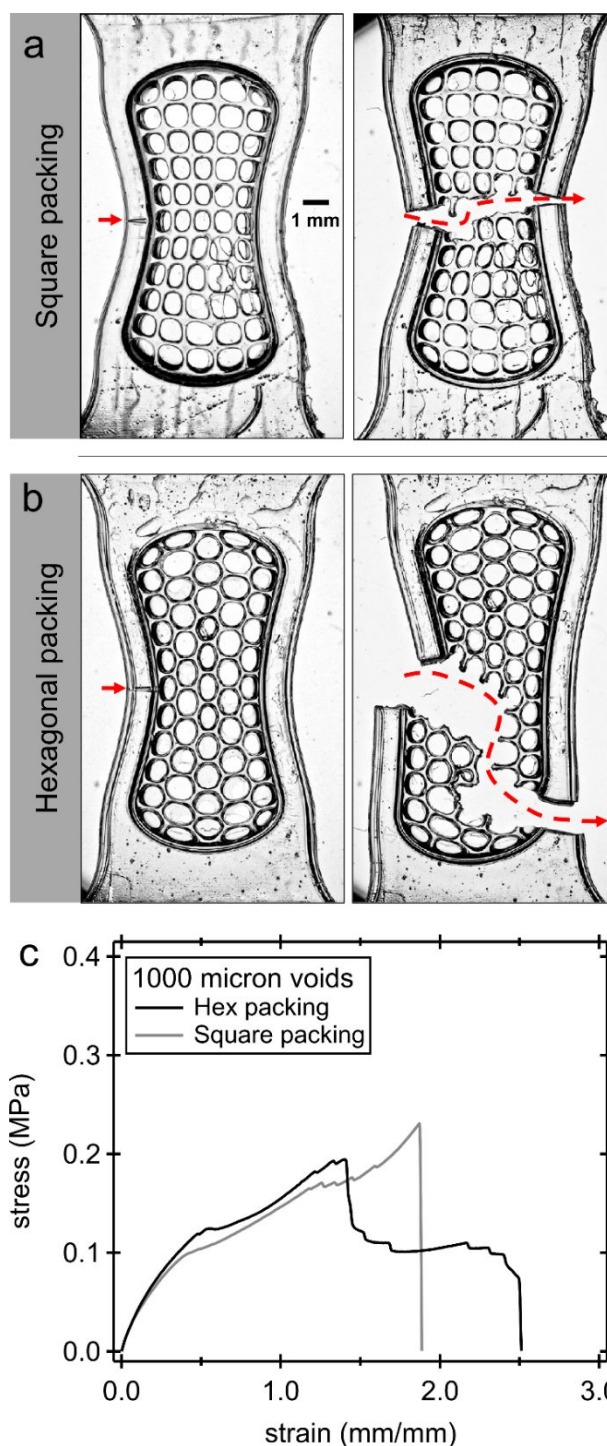


Fig. 4. Summary of results from notched samples, giving access to controlled crack initiation. Optical microscopy images of a) a notched square packed sample and b) a notched hexagonally packed sample with 1000- μm pores before and after being strained to failure. Initial notches and crack paths denoted by arrows and dashed lines, respectively. c) Representative (nominal) stress-strain plot of the two samples, additional results are shown in Fig. S9.

To probe the underlying mechanisms connecting packing geometry and crack tortuosity we turned to 2-D finite element (FE) modelling of square- and hexagonally-packed porous samples

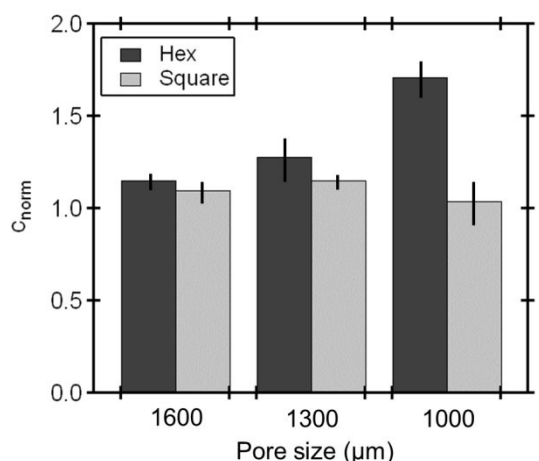


Fig. 5. Impact of pore size and packing of voids on crack tortuosity. Error bars are the result of triplicate runs.

to which tension was applied from 0 to 100% strain in increments of 20% (full details available in the Supporting Information). The principal stresses on the surfaces of the hexagonally- and square-packed samples (pore size = 1600 μm) strained to 100% are illustrated in Fig. 6. The distribution of principal stresses remains roughly unchanged even for smaller pore sizes (Figs. S12-S15). For both geometries, we hypothesize that the regions of highest stress in the porous core guide the crack path, as these are more likely to fracture than low-stress regions, and thus influence the degree of crack tortuosity.

As expected we see packing-dependent differences in maximal stress distribution around each pore. For the square-packed sample strained to 100%, the highest stresses within the core are located at the mid-section of the ligaments perpendicular to the loading axis (Fig. 6a). As such, once a crack traverses the stiff shell and enters the soft core, the thin ligaments between pores bear increasing load and are likely to fail consecutively—leading to linear crack paths perpendicular to the strain axis with little tortuosity. Conversely, the hexagonally-packed specimens display the highest stresses in ligaments oriented at an angle $\theta \approx \pm 60^\circ$ to the axis of strain (Fig. 6b), where the maximum stress between pores was found to be significantly reduced relative to the square-packed example (0.97 and 1.54 MPa respectively). Thus, once a crack traverses the shell into the soft core, it has equal likelihood of fracturing one of two ligaments at either $\pm 60^\circ$ as they bear increasing load. We believe that this initial “fork” in the crack path leads to the deviation from linear crack paths in hexagonally-packed samples and increased tortuosity, as observed. As the crack propagates and encounters additional pores, the stress distribution likely becomes more asymmetric and random, thereby increasing the crack tortuosity as a function of an increasing number of pores encountered across the sample. In an effort to identify possible mechanisms controlling the crack tortuosity in these designs, a simple model was developed (see Supporting Information Section 4C), that demonstrates the important role stochastics likely play in the high degrees of tortuosity observed for hexagonal samples. A full treatment of the crack propagation problem would require analysis of the non-linear mechanical responses, as well as in-plane rotation of the sample during extension, which is beyond the scope of this initial investigation; in the future, such analysis could enable

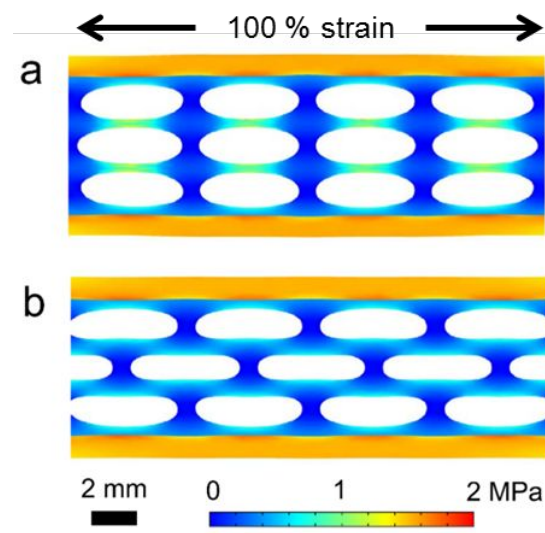


Fig. 6. Summary of results from finite element methods analysis at 100% strain. Color maps of principal stresses on the surface of the (a) square-packed and (b) hex-packed samples. These results are illustrative of the 1600-μm pore diameter samples. The full results for the 1600-μm and 1000-μm pore diameter samples can be seen in Figs. S12-S15.

predictive programming of the failure dynamics using structured material design.

Conclusions

In summary, we employed a novel strategy for multimaterial additive manufacturing to produce polymer-polymer composites with design motifs inspired by nature. By exploiting wavelength-selective polymerization and curing chemistries we printed polymer-polymer composites comprised of a spatially resolved stiff exterior shell and a soft core with well-defined pore sizes/packing. In tension, samples with hexagonally-packed pores of decreasing size demonstrated increased crack tortuosity when compared to samples with square-packed pores, highlighting the importance of pore packing on material performance. The manufacturing strategies and mechanical insights advanced through this work are valuable for the design and development of future resilient multimaterial, polymer-polymer composites. Ongoing research includes the incorporation of micron-sized porogens and hydrogel microparticles into SMA_{LL} resins to further understand property enhancement from three-dimensionally defined, multimaterial systems.

Materials and Methods

Details of resin preparation, sample production, and sample design are described in SI Appendix, Sections 1-2. Experimental protocol and data analysis methods are included in SI Appendix, Section 3. Details of FE simulations are presented in SI Appendix, Section 4.

Data Availability

The research data underpinning this publication are available at <https://doi.org/10.25349/D9P014>.

Conflicts of interest

There are no conflicts to declare.

Author Contributions

L.F.G., N.D.D, C.J.H., and M.T.V. designed research. F.E. and S.H. synthesized diarylethene photoswitches. N.D.D. and R.C. prepared resins and printed samples; L.F.G. tested samples and analysed data. N.C. modelled the behavior of the materials and performed the finite element analysis. L.F.G., N.D.D, N.C., C.J.H., and M.T.V. interpreted results. L.F.G. and N.D.D wrote, and all authors edited, the manuscript.

Acknowledgements

This work was supported by the MRSEC Program of the National Science Foundation through Grant No. DMR-1720256 (IRG-3). N.D.D. was supported by the U.S. Army Research Office under Cooperative Agreement W911NF-19-2-0026 for the Institute for Collaborative Biotechnologies. L.F.G. was partially supported by NSF Grant No. BMAT-1410985. Views and conclusions are those of the authors and should not be interpreted as representing official policies, either expressed or implied, of the U.S. Government. R.C. acknowledges support through the McNair Scholars program. The authors acknowledge the use of the Microfluidics Laboratory within the California NanoSystems Institute, supported by the University of California, Santa Barbara and the University of California, Office of the President as well as the Mechanical Test Laboratory of the UCSB Mechanical Engineering Department. The authors also thank Emmanouela Filippidi for providing the micrograph of the mussel plaque shown in Figure 2a.

References

- H. Gao, B. Ji, I. L. Ja, E. Arzt and P. Fratzl, *Proc. Natl. Acad. Sci. U. S. A.*, 2003, **100**, 5597–5600.
- F. Barthelat and R. Rabiei, *J. Mech. Phys. Solids*, 2011, **59**, 829–840.
- F. Barthelat, *J. Mech. Phys. Solids*, 2014, **73**, 22–37.
- F. Barthelat, Z. Yin and M. J. Buehler, *Nat. Rev. Mater.*, 2016, **1**, 16007.
- J. W. C. Dunlop, R. Weinkamer and P. Fratzl, *Mater. Today*, 2011, **14**, 70–78.
- H. Yuk, T. Zhang, G. A. Parada, X. Liu and X. Zhao, *Nat. Commun.*, 2016, **7**, 1–11.
- S. Lin, C. Cao, Q. Wang, M. Gonzalez, J. E. Dolbow and X. Zhao, *Soft Matter*, 2014, **10**, 7519–7527.
- Y. Huang, D. R. King, W. Cui, L. Sun, H. Guo, T. Kurokawa, H. R. Brown, C. Hui and J. P. Gong, *J. Mater. Chem. A*, 2019, **7**, 13431–13440.
- Y. Huang, D. R. King, T. L. Sun, T. Nonoyama, T. Kurokawa, T. Nakajima and J. P. Gong, *Adv. Funct. Mater.*, 2017, **27**, 1605350.
- N. Suksangpanya, N. A. Yaraghi, R. B. Pipes, D. Kisailus and P. Zavattieri, *Int. J. Solids Struct.*, 2018, **150**, 83–106.
- G. X. Gu, F. Libonati, S. D. Wettermark and M. J. Buehler, *J. Mech. Behav. Biomed. Mater.*, 2017, **76**, 135–144.
- P. Zhang, M. A. Heyne and A. C. To, *J. Mech. Phys. Solids*, 2015, **83**, 285–300.
- A. R. Studart, *Chem. Soc. Rev.*, 2016, **45**, 359–376.
- G. X. Gu, I. Su, S. Sharma, J. L. Voros, Z. Qin and M. J. Buehler, *J. Biomech. Eng.*, 2016, **138**, 021006.
- J. R. Tumbleston, D. Shirvanyants, N. Ermoshkin, R. Januszewicz, A. R. Johnson, D. Kelly, K. Chen, R. Pinschmidt, J. P. Rolland, A. Ermoshkin, E. T. Samulski and J. M. DeSimone, *Science*, 2015, **347**, 1349–1352.
- M. Shusteff, A. E. M. Browar, B. E. Kelly, J. Henriksson, T. H. Weisgraber, R. M. Panas, N. X. Fang and C. M. Spadaccini, *Sci. Adv.*, 2017, **3**, eaao5496.
- M. P. De Beer, H. L. Van Der Laan, M. A. Cole, R. J. Whelan, M. A. Burns and T. F. Scott, *Sci. Adv.*, 2019, **5**, eaau8723.
- B. E. Kelly, I. Bhattacharya, H. Heidari, M. Shusteff, C. M. Spadaccini and H. K. Taylor, *Science*, 2019, **363**, 1075–1079.
- G. I. Peterson, J. J. Schwartz, D. Zhang, B. M. Weiss, M. A. Ganter, D. W. Storti and A. J. Boydston, *ACS Appl. Mater. Interfaces*, 2016, **8**, 29037–29043.
- A. Sydney Gladman, E. A. Matsumoto, R. G. Nuzzo, L. Mahadevan and J. A. Lewis, *Nat. Mater.*, 2016, **15**, 413–418.
- J. O. Hardin, T. J. Ober, A. D. Valentine and J. A. Lewis, *Adv. Mater.*, 2015, **27**, 3279–3284.
- N. D. Dolinski, Z. A. Page, E. B. Callaway, F. Eisenreich, R. V. Garcia, R. Chavez, D. P. Bothman, S. Hecht, F. W. Zok and C. J. Hawker, *Adv. Mater.*, 2018, **30**, 1800364.
- J. J. Schwartz and A. J. Boydston, *Nat. Commun.*, 2019, **10**, 791.
- G. Terrones and A. J. Pearlstein, *Macromolecules*, 2001, **34**, 3195–3204.
- G. A. Miller, L. Gou, V. Narayanan and A. B. Scranton, *J. Polym. Sci. Part A Polym. Chem.*, 2002, **40**, 793–808.
- N. D. Dolinski, Z. A. Page, F. Eisenreich, J. Niu, S. Hecht, J. Read de Alaniz and C. J. Hawker, *ChemPhotoChem*, 2017, **1**, 125–131.
- J. Norman, J. G. Shapter, K. Short, L. J. Smith and N. L. Fazzalari, *J. Biomed. Mater. Res. - Part A*, 2008, **87**, 196–202.
- J. Y. Rho, L. Kuhn-Spearing and P. Zioupos, *Med. Eng. Phys.*, 1998, **20**, 92–102.
- S. A. Ruiz and C. S. Chen, *Stem Cells*, 2008, **26**, 2921–2927.
- Y. Sasai, *Nature*, 2013, **493**, 318–326.
- A. J. Bihendi, B. Altartouri, F. P. Gosselin and A. Geitmann, *Cell Rep.*, 2019, **28**, 1237–1250.
- V. Gordon, L. Bakhtiari and K. Kovach, *Phys. Biol.*, 2019, **16**, 041001.
- T. J. Deming, *Curr. Opin. Chem. Biol.*, 1999, **3**, 100–105.
- J. H. Waite and C. C. Broomell, *J. Exp. Biol.*, 2012, **215**, 873–883.
- J. H. Waite, X. X. Qin and K. J. Coyne, *Matrix Biol.*, 1998, **17**, 93–106.
- J. H. Waite, E. Vaccaro, C. Sun and J. M. Lucas, *Philos. Trans. R. Soc. B Biol. Sci.*, 2002, **357**, 143–153.
- M. H. Wilhelm, E. Filippidi, J. H. Waite and M. T. Valentine, *Soft Matter*, 2017, **13**, 7381–7388.

- 38 E. Carrington and J. M. Gosline, *Am. Malacol. Bull.*, 2004, **18**, 135–142.
- 39 N. Bandara, H. Zeng and J. Wu, *J. Adhes. Sci. Technol.*, 2013, **27**, 2139–2162.
- 40 H. G. Silverman and F. F. Roberto, *Mar. Biotechnol.*, 2007, **9**, 661–681.
- 41 H. Lee, N. F. Scherer and P. B. Messersmith, *Proc. Natl. Acad. Sci.*, 2006, **103**, 12999–13003.
- 42 M. J. Sever, J. T. Weisser, J. Monahan, S. Srinivasan and J. J. Wilker, *Angew. Chemie - Int. Ed.*, 2004, **43**, 448–450.
- 43 Q. Lin, D. Gourdon, C. Sun, N. Holten-Andersen, T. H. Anderson, J. H. Waite and J. N. Israelachvili, *Proc. Natl. Acad. Sci.*, 2007, **104**, 3782–3786.
- 44 N. Holten-Andersen, M. J. Harrington, H. Birkedal, B. P. Lee, P. B. Messersmith, K. Y. C. Lee and J. H. Waite, *Proc. Natl. Acad. Sci. U. S. A.*, 2011, **108**, 2651–2655.
- 45 E. Filippidi, T. R. Cristiani, C. D. Eisenbach, J. Herbert Waite, J. N. Israelachvili, B. Kollbe Ahn and M. T. Valentine, *Science*, 2017, **358**, 502–505.
- 46 N. Holten-Andersen, H. Zhao and J. H. Waite, *Biochemistry*, 2009, **48**, 2752–2759.
- 47 A. Reinecke, L. Bertinetti, P. Fratzl and M. J. Harrington, *J. Struct. Biol.*, 2016, **196**, 329–339.